ROTOR AIRLOADS PREDICTION USING LOOSE AERODYNAMIC/STRUCTURAL COUPLING

Mark Potsdam
Army/NASA Rotorcraft Division
Aeroflightdynamics Directorate (AMRDEC)
U.S. Army Research, Development, and Engineering Command
Moffett Field, CA
mpotsdam@mail.arc.nasa.gov

Hyeonsoo Yeo
Raytheon ITSS
NASA Ames Research Center
Moffett Field, CA
hsyeo@mail.arc.nasa.gov

Wayne Johnson
Army/NASA Rotorcraft Division
NASA Ames Research Center
Moffett Field, CA
wayne.johnson@nasa.gov

ABSTRACT

This work couples a computational fluid dynamics (CFD) code and rotorcraft computational structural dynamics (CSD) code to calculate helicopter rotor airloads across a range of flight conditions. An iterative loose (weak) coupling methodology is used to couple the CFD and CSD codes on a per revolution, periodic basis. The CFD uses a high fidelity, Navier-Stokes, overset grid methodology with first principles-based wake capturing. Modifications are made to the CFD code for the aeroelastic analysis. For a UH-60A Blackhawk helicopter, four challenging level flight conditions are computed: 1) low speed ($\mu = 0.15$) with blade-vortex interaction, 2) high speed ($\mu = 0.37$) with advancing blade negative lift, 3) high thrust with dynamic stall ($\mu = 0.24$), and 4) hover. Results are compared with UH-60A Airloads Program flight test data. Most importantly, for all cases the loose coupling methodology is shown to be stable, convergent, and robust with full coupling of normal force, pitching moment, and chord force. In comparison with flight test data, normal force and pitching moment magnitudes are in good agreement. For the high speed and dynamic stall cases a phase lag in comparison with the data is seen, nonetheless, the shapes of the curves are very good. Overall, the results are a noteworthy improvement over lifting line aerodynamics used in rotorcraft comprehensive codes.

NOTATION

c	blade chord
c_f	skin friction coefficient
C_M	hub moment coefficient
C_T	thrust coefficient
C_W	weight coefficient
M^2c_m	section pitching moment
M^2c_n	section normal force
M_{tip}	hover tip Mach number
M_∞	freestream Mach number
r	radial coordinate
R	blade radius
z	rotor shaft coordinate
α_s	shaft angle, degrees
β_0	coning angle, degrees
β_{1c}, β_{1s}	flapping, longitudinal and lateral, degrees
θ_0	collective angle, degrees
θ_{1c}, θ_{1s}	cyclic, lateral and longitudinal, degrees
μ	advance ratio, M_∞ / M_{tip}
σ	solidity
Ψ	rotor azimuth, degrees (0 aft)

INTRODUCTION

Analysis of helicopter rotors is a challenging multidisciplinary problem. Successful aerodynamic analysis of this problem requires accurate capabilities for modeling unsteady, three-dimensional flowfields, transonic flow with shocks, reversed flow, dynamic stall, vortical wakes, rigid body motion, and deformation. This must be combined with a finite element computational structural dynamics (CSD) analysis. In the fully coupled aeroelastic problem, the aerodynamics and structural dynamics interact and are mutually dependent due to rigid and elastic blade motion, airloads, and rotor trim. To

handle the overwhelming complexity of the problem, rotorcraft comprehensive codes use lower-order aerodynamics models based on lifting line theory and two-dimensional airfoil tables. Airloads predictions using these fast, low fidelity aerodynamic methods often show significant shortcomings.

Bousman [1] identified two key unsolved problems in rotor airloads prediction as 1) the azimuthal phase lag of advancing blade negative lift in high-speed flight and 2) the underprediction of blade pitching moments over the entire speed range. The pitching moment magnitude problem extends into dynamic stall where aerodynamic moment prediction is especially important for pitch link loads estimation. These deficiencies in comprehensive code aerodynamics when applied to various helicopter configurations across a range of flight conditions are well documented [2,3,4]. This was the motivation behind the present work.

The objective of this work is to couple a computational fluid dynamics (CFD) code with a comprehensive rotorcraft analysis in order to make progress in improving rotorcraft airloads prediction capability. The CFD provides high fidelity, nonlinear aerodynamics that is expected to overcome the shortcomings in the comprehensive lifting line aerodynamic analysis. It offers a first principles-based modeling approach for the full flight regime seen on the rotor disk and in the wake. The comprehensive code continues to perform the structural dynamics and trim calculations. Furthermore, an efficient loose coupling approach is taken with the objective of documenting convergence behavior and identifying any shortcomings that might warrant alternative procedures. A range of challenging flight test conditions, high speed with advancing blade negative lift, low speed with blade-vortex interaction, high thrust with dynamic stall, and hover, is used to reach conclusions regarding the appropriateness of the CFD and coupling methodologies. The focus of the work is on airloads prediction — normal force and pitching moment. At this time, performance prediction is not an objective.

BACKGROUND

Coupling between CFD and rotorcraft comprehensive codes has been accomplished in two ways. In the loose (weak) coupling methodology, information between CFD and CSD is transferred on a per revolution, periodic basis. In the tight (strong) coupling approach, the CFD and CSD codes are coupled at every time step and integrated simultaneously. Although tight coupling is more rigorous, care must be taken to ensure timewise accuracy between CFD and CSD, and code modification may be required for efficient process communication. Rotor trim for the tight coupling methodology is problematic. On the other hand, loose coupling allows for a modular approach and communication through file input/output. Each discipline handles its time accuracy as required. Trim is a natural result of the periodic comprehensive analysis.

It remains to be seen if loose coupling has any unexpected drawbacks. An excellent comparison of the two coupling approaches using the CFD codes FLOWer and WAVES and comprehensive code HOST was made by Altmikus [5]. A 2.5 times increase in cost for the tight coupling was indicated while yielding very similar solutions for high speed forward flight conditions. Trim was expediently obtained in a weak coupling fashion. Pomin [6] used overset methods and deformable grids in a tight coupling procedure but avoided the trim issue by fixing control angles.

A well-known loose coupling procedure was developed by Tung, Caradonna, and Johnson [7] using a transonic small disturbance (TSD) code. Other TSD [8] and full potential methods [9,10,11] were later coupled. These CFD methods require inflow angles from the comprehensive code to account for structural deformation, through surface transpiration instead of grid deformation. The inflow angles also include the influence of the wake outside the CFD domain, usually limited to the outboard part of the blade and several chords away. Full potential solutions coupled section lift and, with some difficulty, moments, which were shown to have an important effect on torsion prediction. Issues were encountered with convergence [8,10] and complex boundary conditions [9].

With the continual advancement of high speed computers, it has become possible to use Euler [5,12] and Navier-Stokes [13,14,15,16] CFD in the coupling. Full domain Navier-Stokes analyses do not require the added complexity of inflow angles to model the wake, instead relying on direct simulation of the farfield and all rotor blades. In general, this requires the use of multiblock or overset meshes. Sitaraman [13], however, solves only the near-field of a single blade and uses fast Biot-Savart evaluation methods to apply induced velocities at all the grid points, where the induced velocities are computed from a free wake model. Researchers at the University of Maryland have made considerable progress in understanding the vibratory airloads of the UH-60A high speed, forward flight test point. Unfortunately, a CFD boundary condition error in TURNS [16] requires that previous results [13,14] be re-examined. Pahlke [15] shows improved correlation on the 7A and 7AD model rotors in high speed forward flight with the FLOWer CFD code only when viscous effects are included. A small advancing side phase lag (10-15 degrees) is seen, but normal force magnitudes are well predicted. Pitching moment magnitudes and shapes are less than satisfactory.

METHODOLOGY

CAMRAD II

Structural dynamics and rotor trim for the coupled calculations are performed using the comprehensive rotorcraft analysis CAMRAD II [17]. In this work an isolated rotor is modeled as a flexible blade with nonlinear finite elements.

The CFD/CSD coupled solutions are compared with state-of-the-art comprehensive analysis-only results. The aerodynamic model in CAMRAD II is based on second-order lifting line theory. The blade section aerodynamic modeling problem in lifting line theory is unsteady, compressible, viscous flow about an infinite wing in a uniform flow consisting of a yawed freestream and wake-induced velocity. This problem is modeled within CAMRAD II as two-dimensional, steady, compressible, viscous flow (airfoil tables) plus corrections for swept and yawed flow, spanwise drag, unsteady loads, and dynamic stall. The wake problem of lifting line theory is an incompressible vortex wake behind the lifting line, with distorted geometry and rollup. The wake analysis calculates the rotor non-uniform induced velocity using a free wake geometry. The tip vortex formation is modeled. The model in CAMRAD II is generally second-order accurate for section lift, but less accurate for section moments.

OVERFLOW-D

The CFD calculations use the Reynolds-averaged Navier-Stokes computational fluid dynamics code OVERFLOW-D [18]. It is based on the OVERFLOW 1.6au code, which has been continually developed at NASA and has been applied to a wide range of fluid dynamics problems. OVERFLOW-D includes major modifications for time-dependent, rigid body motion of components, in particular individual moving rotor blades which are often required for complex rotorcraft configurations. Previous work has validated the code for aerodynamic performance predictions of rigid blade helicopter and tiltrotor configurations in hover [19,20]. This work extends the validation to helicopter airloads in edgewise forward flight.

OVERFLOW-D solutions are computed on structured, overset grids using body-conforming "near-body" grids and automatically generated Cartesian "off-body" grids [21]. Near-body grids are used to discretize the surface geometries and capture wall-bounded viscous effects. Off-body grids extend to the farfield with decreasing grid density and capture the wakes. User-defined subroutines prescribe the arbitrary six degree-of-freedom motion. The grid motion necessitates recalculation of the domain connectivity, including hole cuts and intergrid boundary point (IGBP) interpolation coefficients, at each time step as the near-body grids move through the stationary off-body grids. Hole cutting, which is required when one grid passes through another, is performed efficiently using the object X-ray technique [22]. Interpolation coefficients are determined using inverse maps and Newton iteration searching. Reuse of information from the previous time step enables an order of magnitude speed-up compared to domain connectivity solutions from scratch. Using this technique, the domain connectivity work can be efficiently performed in less than 20% of the time required for the flow solver.

Because of the aeroelastics of the coupled solutions, several modifications are made to the rigid body version of OVERFLOW-D. Capability that has been added to accurately account for deforming grids includes implementation of the Geometric Conservation Law and finite volume time metrics, surface grid deformation and volume grid movement, and regeneration of X-rays and inverse maps.

Geometric Conservation Law

In order for fluid dynamics conservation laws that use body conforming coordinate transformations to maintain global conservation, spatial and temporal grid metrics must satisfy certain geometric identities. In differential or integral form the restriction is similar to mass conservation and is known as the Geometric Conservation Law (GCL) [23]. The GCL is related to the ability of a numerical scheme to preserve the state of a uniform flow. Grid metrics with this property are called freestream preserving. Satisfying these conditions may improve the stability and spatial and/or temporal accuracy of the CFD algorithm [24].

For steady flows, freestream capturing spatial grid metrics can be formulated using a finite volume point of view. OVERFLOW-D has long used such second-order accurate formulas. For unsteady calculations to date, time metrics in OVERFLOW-D have used finite difference formulas that are not freestream preserving. For rigid motion calculations the error introduced is often small and can be treated with freestream subtraction in the flux differences.

In order to improve the time accuracy of OVERFLOW-D and rigorously implement aeroelastically deforming grids, second-order accurate, freestream preserving, finite volume time metrics have been formulated and used [25]. While higher-order freestream preserving spatial and temporal grid metrics can be devised, they are expensive to calculate at every step of an unsteady, moving body problem. So, in addition, a source term representing the GCL has been added to the right

hand side of the discretized Navier-Stokes equations to more accurately represent the governing equations when the GCL is not satisfied by the metrics [26].

Grid Deformation

In addition to rigid body movement of the rotor blades due to rotor rotation, collective, cyclic, and elastic motion is introduced by the structural mechanics and dynamics. Modifications are made to OVERFLOW-D to allow the blade grids to aeroelastically deform. Given the nature of overset grid generation, it is important that the implementation handle general grid topologies.

First, the surface grids defining the blades are deformed. The motions from CSD are specified as three translations and three rotations of the undeflected blade quarter chord as a function of radius, r/R, and azimuth, Ψ. These six motions completely contain all the control inputs, elastics, and dynamics, while also taking into account any geometric quarter chord variations (for example, tip sweep). All blade deformations are modeled here except for airfoil chord deformations. Blade surfaces are automatically detected based on flow solver boundary conditions. Any point on the blade surface can be transformed, based its local value of r/R and the current blade azimuth angle, through two-dimensional interpolation of the CSD motions. If C-meshes happen to be used, the points on the wake cut are handled naturally in the same manner. Cubic spline interpolation is employed in order to maintain C^1 continuity of the motion derivatives, which are related to the grid speeds. Surface point motion is finally computed from a 3x3 transformation matrix that contains both the translational and rotational motions.

Second, the volume grid is adjusted to account for the surface motion. Again, no restrictions are made for particular grid topologies, such as planar grid sections. Field points are moved using the transformation matrix of the associated constant computational coordinate surface point. Through the built-in rotation of the surface point that is transmitted to the field points, grid quality is maintained, including any initial orthogonality [26]. Because IGBP interpolations are recalculated for overset, moving body problems, there is no savings in specifying that the blade near-body grid outer boundary not move. In fact, any moderate amount of rotor blade flapping requires that the outer boundary deflect in concert with the surface. Outer boundaries of near-body grids are typically only one chord length from the blade surface. The algebraic nature of the calculation makes the cost for high quality grid deformation relatively low. This scheme handles reasonable rotor blade motions. Following the surface and volume grid deformation due to aeroelastics, the rotor rotation about the azimuth is added.

X-rays and Inverse Maps

For static geometries and rigid body motion, the shape of the "hole" that the geometry makes with respect to other grids remains fixed, although because of grid motion the hole location is not fixed in time. For deforming geometries neither the hole shape nor location is fixed. Using the object X-rays technique, deforming surface geometries should be re-X-rayed to accurately represent the surface, particularly as previously noted due to flapping. Modifications to OVERFLOW-D integrate the X-ray software, GENX, as runtime subroutines. X-rays are recomputed at a user-defined interval, for example, every 2–5 degrees of azimuth. Although the relative cost compared with a flow solver time step is large since the GENX software is not parallelized, recalculation intervals of at least 25 time steps minimize the overall cost.

At the same re-X-raying interval, inverse maps are also recomputed. They are required to determine initial guesses for IGBP donor searches in near-body grids. Given X,Y,Z coordinates of an IGBP, inverse maps return approximate J,K,L computational coordinates in a donor grid. However, using OVERFLOW-D's efficient n^{th}-level restart capability for intergrid interpolation, the inverse maps are only needed when an initial guess based on the previous time step is incorrect. Again, the cost of generating the inverse maps is amortized over several time steps, although their generation is parallelized. Serial inverse map computation in an overset method using tight coupling [27] was found to be quite costly.

Parallel Computing

Solutions are computed on large parallel computers or a network of PCs/workstations communicating with the Message Passing Interface (MPI) protocol. Both the domain connectivity and flow solver modules have been parallelized for efficient, scalable computations using MPI. Coarse grain parallelization on large numbers of processors is achieved by distributing grids among the processors, and, if necessary, splitting them as appropriate into smaller blocks to prevent bottlenecks. Boundaries that are created in the splitting process have explicit boundary conditions, similar to intergrid boundaries of the original grid system.

Coupling

A loose coupling strategy based on a trimmed, periodic rotor solution is employed. The coupling methodology is an incremental formulation developed previously [7] and outlined in Figure 1. In summary, in an iterative fashion the methodology replaces the comprehensive airloads with CFD airloads while using

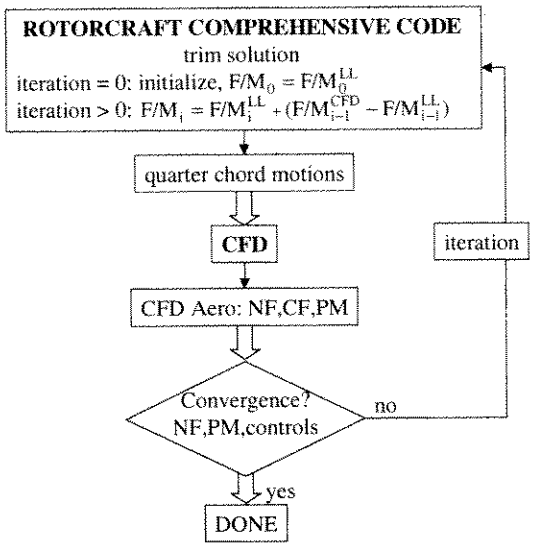

Figure 1. Flow diagram for CFD/CSD loose coupling procedure (F/M = forces and moments)

lifting line aerodynamics to trim and CSD to account for blade deformation.

The coupling calculation is initialized with a comprehensive analysis using lifting line aerodynamics, resulting in a trimmed rotor solution. This run creates initial quarter chord motions as a function of radius and azimuth, which are transferred to the CFD. Because OVERFLOW-D models the full rotor domain, including all blades and the wake, there are no other required inputs from the comprehensive code to CFD. This is unlike potential flow or Navier-Stokes partial domain methods [9,13] that require a description of the wake from the other blades and in the farfield, introduced via partial angles or induced velocities.

The CFD code is run using the specified motions. This initial CFD solution need not be fully converged, and typically, for a 4-bladed rotor in forward flight, 1 to 1¼ rotor revolutions is sufficient. OVERFLOW-D outputs the surface grid and flow variables at user-specified intervals, typically every 5 degrees. It is not necessary or desirable to save the complete flowfield at this interval. The surface files are post-processed to obtain normal force (NF), pitching moment (PM), and chord force (CF) as a function of radius and azimuth. Only the pressure components of the forces are calculated for the present paper. Viscous components of the NF and PM are negligible, and the viscous CF effect will be investigated. For completeness and future performance and structural loads predictions, viscous forces should be added to the post-processing software. NF, PM, and CF are passed to the comprehensive code for the next coupling iteration.

Thereafter, the aerodynamic forces and moments (F/M) that are used in the comprehensive code at the next iteration (i) are the comprehensive lifting line (LL) solution required to trim plus a correction based on CFD.

$$F/M_i = F/M_i^{LL} + (F/M_{i-1}^{CFD} - F/M_{i-1}^{LL}) \qquad (1)$$

That is, the correction is the difference between the previous CFD and comprehensive lifting line solutions. Alternatively, the equation can be written as

$$F/M_i = F/M_{i-1}^{CFD} + (F/M_i^{LL} - F/M_{i-1}^{LL}) \qquad (2)$$

Then it is seen that the forces and moments used in the comprehensive code are those computed by CFD plus an increment required to retrim the rotor. The trim correction should, in general, be small, and all that is required is that the trends of the table look-up be relatively consistent with the CFD. There is a possibility that while trying to trim, the lifting line aerodynamics will move the solution in wrong direction. This might be expected when parts of the rotor are stalled. However, for all the cases demonstrated here, no convergence difficulties were encountered. Currently, it is computationally prohibitive to use CFD inside the trim loop.

With new quarter chord motions of the retrimmed rotor, the CFD is rerun. Again, it is not necessary to fully reconverge the flow solution, resulting in a form of relaxation. If the previous CFD calculation is used as a restart condition, for a 4-bladed rotor, ¼ of a revolution is sufficient.

The coupled solution is converged when collective and cyclic control angles and CFD aerodynamic forces do not change between iterations. Plotting accuracy of aerodynamic forces and moments and 3 significant figures for control angles have been used here. Upon convergence the total airloads used in the comprehensive code are the CFD airloads. This can easily be seen from the above equations, since at convergence F/M^{LL} does not change between iterations i and i-1 because no trim or aeroelastic changes are required. All trim constraints are satisfied by the final CFD solution. If the parameters are not converged, the next coupling iteration begins again with the comprehensive analysis.

Coupling Implementation

The coupling between CAMRAD II and OVERFLOW-D has been seamlessly integrated with UNIX scripts and FORTRAN post-processing codes. CAMRAD II outputs a blade motion file describing the undeflected quarter chord and three translations and three rotations of the deflected quarter chord, as a function of radius and azimuth. OVERFLOW-D reads this file as input and computes the next revolution with these

motions. Post-processing codes extract the CFD airloads from surface files. The CFD airloads along with the total airloads from the previous iteration are used to create a "delta" file. The correction is implemented in the comprehensive analysis as an input increment $\Delta F/M$

$$F/M_i = F/M_i^{LL} + \Delta F/M_i \qquad (3)$$
$$\Delta F/M_i = \Delta F/M_{i-1} + (F/M_{i-1}^{CFD} - F/M_{i-1})$$

The increment is updated from the difference between the CFD loads and the total comprehensive analysis loads. In this manner, it is not necessary to separate out the lifting line portion.

CAMRAD II uses the delta file as input for the next iteration. This modular approach using minimum input/output files allows for the comprehensive or CFD code to be easily substituted. An example of this modularity is illustrated later.

For efficient, automated coupling, both CAMRAD II and OVERFLOW-D run on the same computer. The cost of the comprehensive solution is at least 2 orders of magnitude less than the CFD, so CAMRAD II has not been parallelized. The CFD code is stopped and started for each coupling iteration at a user-specified frequency. The startup cost is relatively insignificant due to the large number of time steps to obtain a quasi-reconverged solution. This obviously would not be the case for a tight coupling strategy, where the CFD and CSD codes would have to be more closely integrated by means other than file input/output.

UH-60A CONFIGURATION AND MODELING

Flight Test Data

A unique and extensive flight test database exists for a UH-60A helicopter in level flight and transient maneuvers [28]. The data were obtained during the NASA/Army UH-60A Airloads Program. The database provides aerodynamic pressures, structural loads, control positions, and rotor forces and moments, allowing for the validation of both aerodynamic and structural models. The test matrix contains a range of advance ratios and gross weight coefficients, as shown in Figure 2, with the test points investigated here indicated. The focus of this paper is on airloads prediction. Absolute pressures were measured at r/R = 0.225, 0.40, 0.55, 0.675, 0.775, 0.865, 0.92, 0.965, and 0.99 (Figure 3) along the blade chord and integrated to obtain normal force, pitching moment, and chord force.

The data have undergone a significant amount of careful investigation [29], however, some discrepancies have not yet been resolved. Measured rotor thrust was determined from the gross weight of the helicopter plus estimates for the fuselage and tail rotor loads. Measured hub moments, roll and pitch, were determined from an upper shaft bending moment gauge. However, integration of the measured pressures over the rotor result in poor agreement with measured thrust and moments. For example, for the high speed test point, the integrated thrust is 10% higher and the total integrated hub moment is 50% larger with an 80-degree phase difference compared to the measured values. Consequently, it is clear that there is some uncertainty in the aircraft trim condition, and there will be some discrepancy in comparison of mean airloads values [30]. This is a common problem in rotorcraft experimental testing, e.g. Lorber [31]. Errors in the blade pressures can have large effects on integrated section pitching moments. Bad trailing edge pressure taps have been discovered in this dataset that considerably skew the pitching moment mean values. For this reason, all plots of pitching moment have the mean removed.

Comprehensive Modeling

The UH-60A master input database, available to approved researchers, has been used to define the elastic UH-60A 4-bladed rotor model. The database contains geometric, aerodynamic, and structural material properties. Figure 3 shows the blade planform and pressure transducer locations. The blade has a radius of

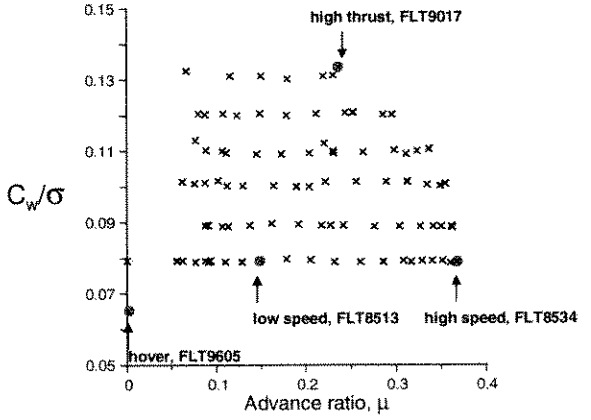

Figure 2. UH-60A Airloads Program level flight test matrix

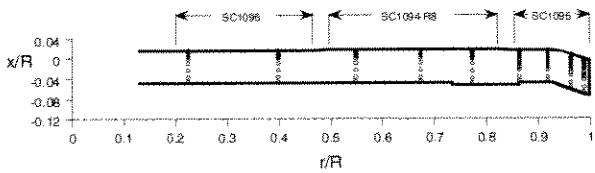

Figure 3. UH-60A blade planform

322 inches, and the swept tip begins at r//R = 0.929. The solidity, σ, is .0826, and there is about −16 degrees of nonlinear twist. Further details of the blade can be found in [29].

The comprehensive analysis trim solution for forward flight corresponding to the UH-60A flight test data solves for the collective and cyclic controls required to obtain the specified (measured) thrust and shaft pitch and roll moments with fixed rotor shaft angle. Of course, other trim conditions, such as full vehicle trim or specified flapping of wind tunnel models, could be used in the coupling.

For the CFD/CSD coupling, all aerodynamics are eventually determined by CFD. Therefore, it is most efficient to use the fastest possible wake model in the comprehensive code, i.e. uniform inflow. Higher-order wake models might result in a better initial solution, but there is no advantage for later coupling iterations. Additional aerodynamic models that alter the input CFD aerodynamics are turned off, such as a tip-loss model.

For comparison of the coupled results with state-of-the-art comprehensive analysis, a multiple trailer consolidation wake model with standard parameters is used [4]. An ONERA EDLIN dynamic stall model [17] is turned on for the high thrust case. The consolidation model used a constant vortex core size value of 50% chord. A 15-degree azimuthal step size is standard for the aerodynamic and structural dynamic calculations in CAMRAD II. This limits the harmonic content of the blade motions to 12/rev, while the aerodynamics contains much higher frequencies.

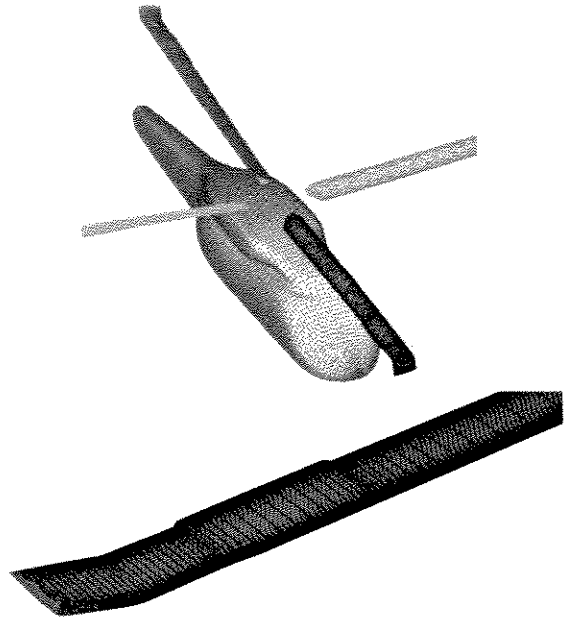

Figure 4. UH-60A configuration coarse surface grids

CFD Modeling

A theoretical UH-60A CFD blade grid was developed using the master database. Definitions of the SC1095 and SC1094R8 airfoils have been combined with twist, chord, quarter chord location, and trim tab distributions to generate the rotor blade definition. Realistic tip cap and root definition have also been used. The blunt trailing edge airfoils have been closed for ease of grid generation. Two-dimensional results indicate this is a reasonable approximation for these airfoils [32].

Grid generation uses the overset near-body/off-body discretization concept. For each of the 4 blades, 3 near-body grids define the blade, root cap, and tip cap. They extend about one chord away from the surface and include sufficient resolution to capture boundary layer viscous effects. Blade and cap grids use a C-mesh topology. The main blades have dimensions of 249x163x65 (chordwise, spanwise, normal). The chordwise leading and trailing edge spacings are 0.001 and 0.002 chords, respectively, with 201 points on the airfoil surface. The first three points at the blade surface have a constant spacing, calculated to produce a $y+ \leq 1$. The surface grids of the 4-bladed configuration and an undeflected blade are shown in Figure 4. The fuselage grid is also shown, although most solutions do not include the fuselage.

Off-body Cartesian grid generation is automatically performed by OVERFLOW-D. The finest off-body spacing for the baseline grid is 0.10 chords. This level-1 grid surrounds the blades and extends ±1.2R in x and y and ±0.3R in z. It is manually specified in order to contain a portion of the wake. It must be emphasized that a typical wake vortex core size is 0.10 chords, and, therefore, significant dissipation of the wake vortex cores will occur. A total of five progressively coarser levels are generated out to the farfield boundary, which is placed at 5R in all directions from the center of the domain. The grid spacings differ by a factor of two between each Cartesian mesh level.

The baseline grid contains 26.1 million (M) points: 14.4M near-body (55%) and 11.7M off-body (45%). A coarse grid with $1/8^{th}$ the number of points extracted from the baseline grid is also used in this work. Where grid points of overset meshes fall inside the geometry, hole cutting is employed to blank out these points. A cut through the grid system in Figure 5 shows the deflected near-body grids (blue), level-1 (red) and higher (black) Cartesian off-body grids, hole cuts, and grid overlap. The baseline grid uses double fringing overlap, while the coarse grid uses single fringing. Double fringing allows derivatives as well as flow variables to be smoothly transferred between overlapped grids. Due to stability limitations, an azimuthal step size of 0.05 degrees is used

in all CFD calculations, corresponding to 1800 iterations per 90 degrees of rotation of the 4-bladed rotor.

The OVERFLOW-D runs use 2nd-order spatial central differencing with standard 2nd and 4th-order artificial dissipation and an implicit 1st-order temporal scheme in the near-body grids. The Baldwin-Barth one-equation turbulence model is employed in the near-body grids, which are assumed fully turbulent. Fourth-order spatial with reduced artificial dissipation, explicit 3rd-order temporal, and inviscid modeling are used in the off-body grids, all to minimize as much as possible any wake diffusion.

RESULTS

Four level flight UH-60A data points have been used to test the loose coupling procedure and are documented in Table 1. Using these test points, the accuracy, efficiency, and robustness of the CFD/comprehensive coupling procedure will be demonstrated. Additionally, the aerodynamics will be investigated through airloads comparisons and flowfield visualization.

Table 1. UH-60A flight test counters

Counter	C_T/σ	μ	M_∞	M_{tip}	α_s (deg)
c8534	0.084	0.37	0.236	0.642	-7.31
c8513	0.076	0.15	0.096	0.644	0.76
c9017	0.129	0.24	0.157	0.665	-0.15
c9605	0.066	0.003	hover	0.650	

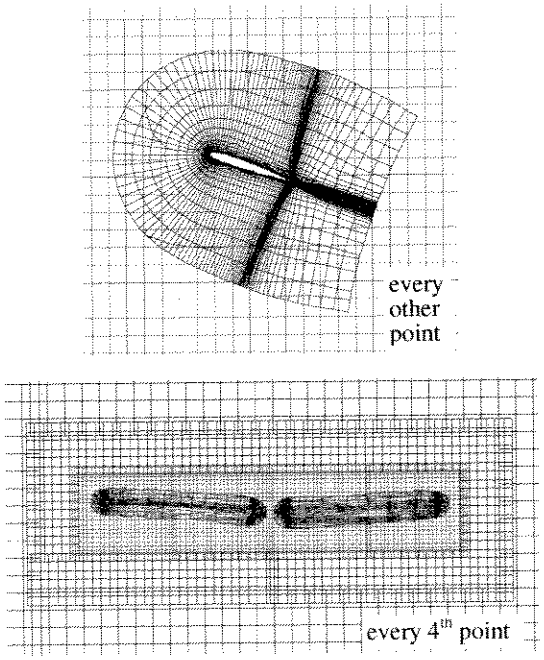

Figure 5. UH-60A baseline volume grid

High Speed

Flight counter c8534 is a high speed, $\mu = 0.37$, level flight data point. The hover tip Mach number of the UH-60A is approximately 0.64. The freestream Mach number of this point is 0.236. Many investigations have been performed on this flight test counter in order to understand unsolved analysis problems of the advancing blade azimuthal phase lag and underprediction of blade pitching moments [1].

Coupling Convergence

Representative airloads convergence on the baseline grid is shown in Figure 6. The normal force (M^2c_n) and pitching moments (M^2c_m) have converged to plotting accuracy in 6 iterations. The coupling frequency is 90 degrees for the 4-bladed rotor. The smooth solutions at 90, 180, and 270 degrees azimuth indicate this to be an accurate and efficient strategy. The advancing side negative loading is the last area to converge. This fast convergence of the loose coupling methodology is in agreement with previous studies [5,8].

Figure 7 shows convergence of the CAMRAD II control angles and trim targets, normalized by their final values. The thrust and moment trim values from CFD do not converge to the exact CAMRAD II specified trim targets due to coarser azimuthal and radial discretization and interpolation of the CFD data within the comprehensive code. Also, a large 15-degree azimuthal

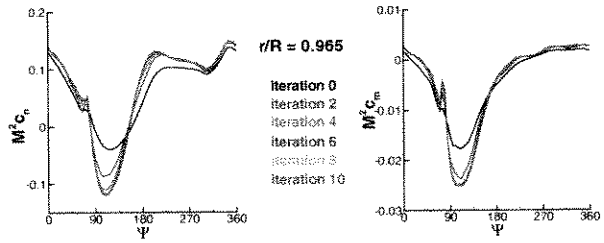

Figure 6. Airloads convergence, $\mu = 0.37$

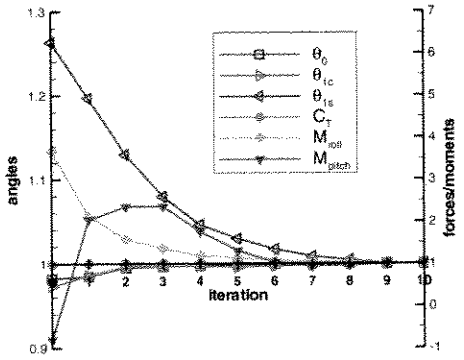

Figure 7. Trim target and controls convergence, $\mu = 0.37$

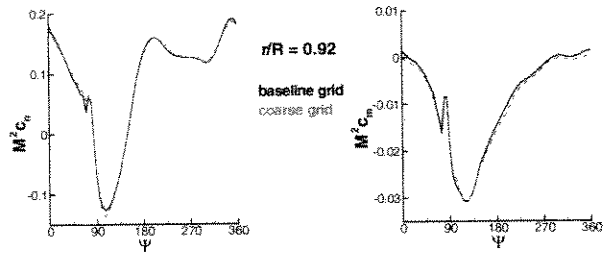

Figure 8. Grid convergence, $\mu = 0.37$

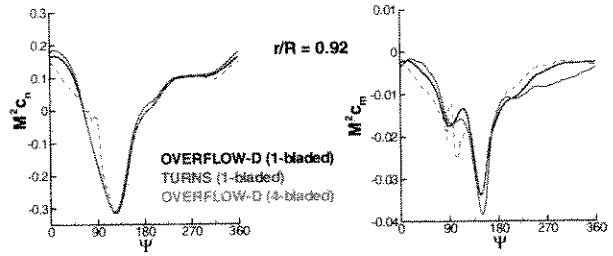

Figure 9. CFD code comparison and wake effect, $\mu = 0.37$

step size in CAMRAD II, compared with 0.05 degrees in the CFD, implies that high frequency oscillations in the CFD airloads may not be taken into account. Except for this, OVERFLOW-D and CAMRAD II airloads do converge to the same values, as expected.

Grid Effects and CFD Code Comparison

A coarse grid, derived by taking every other point from the baseline grid, has been used to investigate grid convergence of the coupled results. Figure 8 shows airloads comparisons at the span station with the largest difference. For this data point, the coarse grid gives almost the same airloads at approximately $1/8^{th}$ the cost. A comparison of converged control angles for the two coupled solutions are shown in Table 2, indicating good agreement. Coupling convergence histories are similar for the two grid densities as well.

Table 2. Comparison of converged control angles (degrees) as a function of grid density

grid	θ_0	θ_{1c}	θ_{1s}	β_0	β_{1c}	β_{1s}
baseline	14.6	-8.63	2.39	3.43	0.70	2.04
coarse	14.8	-8.61	2.44	3.43	0.71	2.03

Although the wake is poorly resolved in the coarse grid due to large level-1 off-body spacing (20% chord), the airloads for this high speed case are not sensitive to the wake details. The rotor wake is quickly convected past the rotor, which has a relatively large nose down shaft angle. Figure 9 justifies this assertion. A comparison is made between the full, 4-bladed configuration with wake modeling on the coarse grid and a simplified analysis that uses only one isolated, inviscid, coarse grid blade. The wakes from the other blades and the farfield are not contained in this 1-bladed solution. Both solutions use the same fixed set of quarter chord motions. It is clear that for the high speed data point, there is limited wake interaction only in the first quadrant. Similar conclusions are drawn by Pahlke [15] for the 7A model rotor. Most importantly, the wake has no effect on the phase of the advancing side negative loading. These calculations and computed Euler vs. Navier-Stokes comparisons (not shown) also indicate that viscous effects are not important, unlike results reported by Pahlke, which were quite sensitive to boundary layer effects.

Also shown in Figure 9 is the 1-bladed result from the TURNS CFD code [16], which uses upwind spatial and 2^{nd}-order temporal algorithms. In spite of numerous code differences, the agreement between OVERFLOW-D and TURNS is quite satisfying, helping to validate the implementation of the aeroelastic deformation in both codes.

Several flow solver parameters were investigated to determine airloads prediction sensitivity. Reduced artificial dissipation and higher-order spatial differencing in the near-body grids and reduced azimuthal step size ($\Delta\Psi = 0.025$) all showed no effect on the airloads for the baseline grid. Additionally, results here were not sensitive to the time metric formulation or even satisfaction of the GCL.

Data Comparison

Comparisons of the coupled OVERFLOW/ CAMRAD results with flight test data and CAMRAD II free wake analysis are shown in Figure 10 for representative span stations. These results are trimmed to the measured thrust and upper shaft bending moments. The magnitudes of the normal force and especially the pitching moment from the coupled solution are in good agreement with the flight test data. Recall that the mean has been removed from the pitching moment. A 25-degree phase shift exists in the airloads in the first and second quadrant, persisting into the third, but the shape of the airloads curves are excellent. The shape of the vibratory normal forces, 3/rev and higher, are in equally good agreement but also suffer from a phase lag and modest underprediction of magnitude. Small oscillations in the test data in the first quadrant resulting from the wake as the blade approaches 90 degrees azimuth are beginning to be captured in the coupled solution.

The phase and magnitude of the coupled airloads are significantly improved over the free wake analysis. The underprediction of advancing blade pitching moments has been remedied and the negative lift phase lag has been

reduced. The magnitude of the vibratory forces are also improved.

Qualitative comparisons of normal force on the rotor disk are shown in Figure 11. It is seen that the overall comparison as well as some of the details are quite good, although the phase lag is again apparent.

Computational and experimental comparisons of the mean normal force distributions as a function of radius are shown in Figure 12. Two coarse grid coupled solutions are shown, trimmed to the measured ($C_T/\sigma = 0.084$) and integrated thrusts ($C_T/\sigma = 0.094$). Neither show particularly good agreement with test data. The CAMRAD II free wake span loading indicates much higher tip loading. This plot highlights the importance of

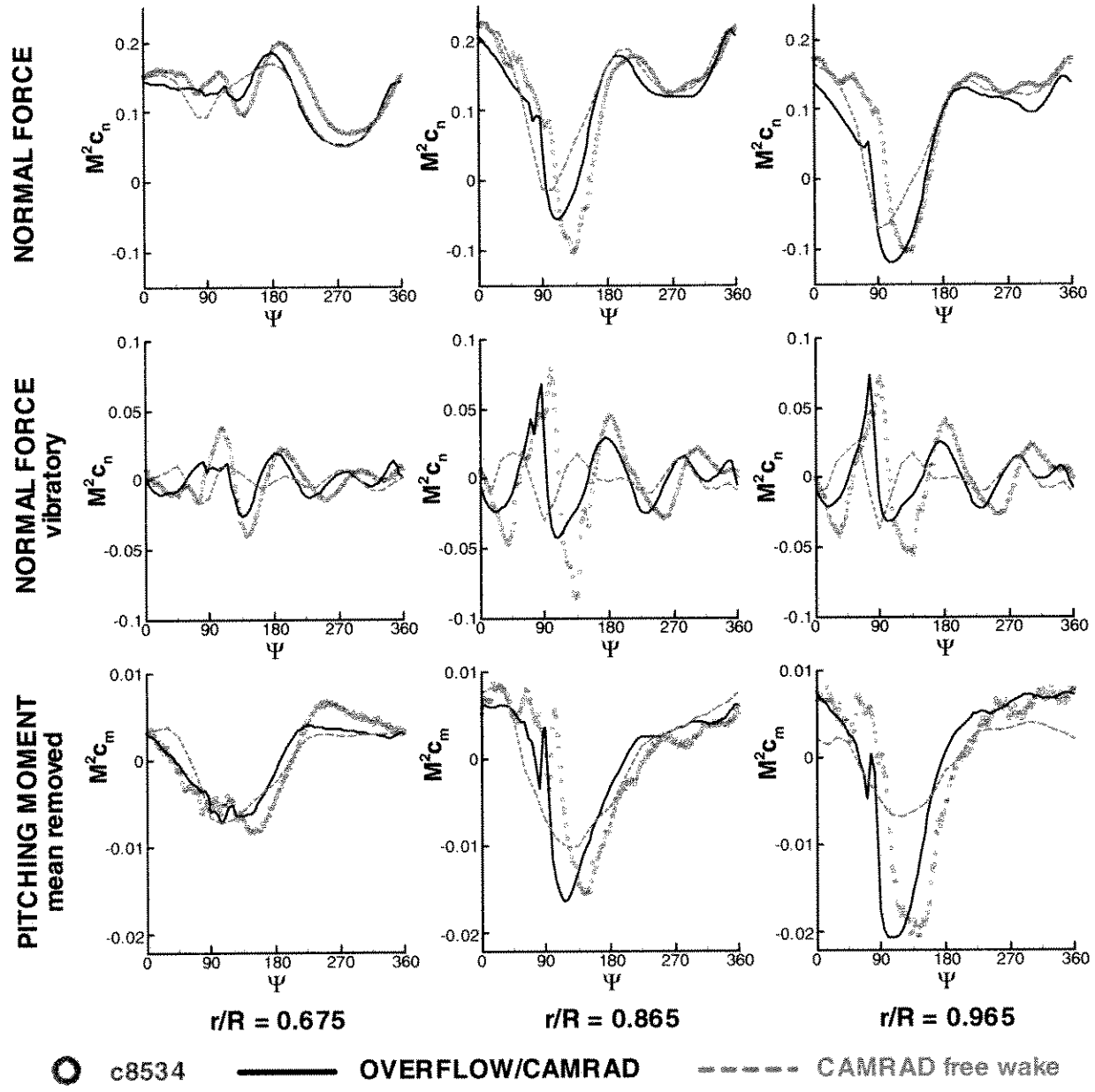

Figure 10. Airloads comparison, $\mu = 0.37$

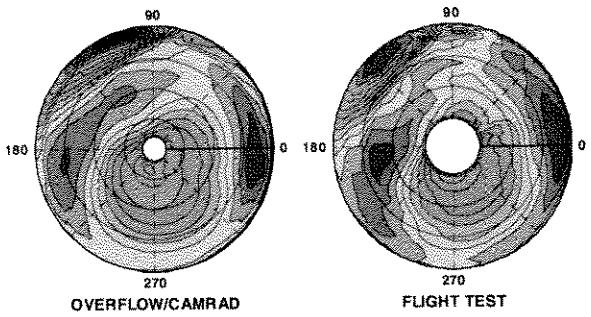

Figure 11. Rotor disk normal force comparison, $\mu = 0.37$

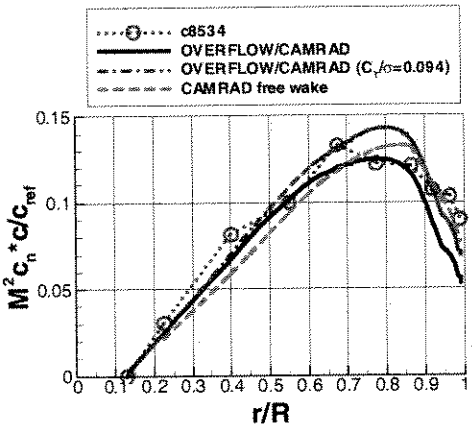

Figure 12. Mean normal force distribution, $\mu = 0.37$

determining the actual thrust on the rotor and the trim condition in general. Based on a lack of smoothness in the test data, some radial stations are probably in error, but the causes cannot be determined. Some but not all of the thrust discrepancy may be attributed to inaccurate estimates of fuselage and tailplane download.

Discussion

Changing the moment trim target, phase or magnitude, has an effect on the calculated airloads phase, magnitude of the negative loading, and wake interactions. Figure 13 shows the effect on normal force at representative stations due to varying the phase of the measured moment (C_M = 0.00011, phase = 111 degrees). The integrated airloads hub moment (C_M = 0.00017, phase = -9 degrees) has a 50% higher magnitude and 120 degree phase difference compared with the measured values. This again shows the sensitivity of the coupled solutions to flight test trim quantities with unknown accuracy.

Because the current coupling post-processing only includes forces and moments due to pressure, a constant section drag coefficient, based on two-dimensional CFD airfoil calculations [32], was added to the calculated chord

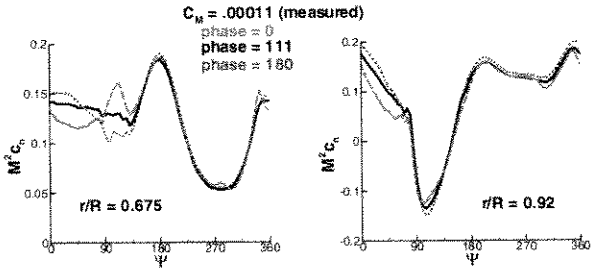

Figure 13. Hub moment phase effect on airloads, $\mu = 0.37$

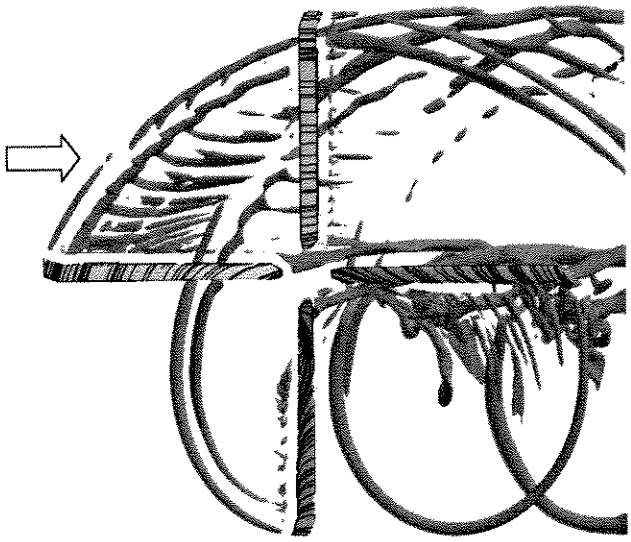

Figure 14. Wake visualization and surface streamlines, $\mu = 0.37$

force. No discernable changes are noted in the airloads other than a small (~1 degree) increase in the lag angle.

Visualization of the wake in Figure 14, using the Q-criteria [33], highlights several interesting structures. Throughout almost the complete azimuth, the blades shed vorticity from the tip and near the sweep break. This indicates the appropriateness of dual peak or multiple-trailer wake models. A coalescence of vortices around 90 degrees azimuth accounts for the airloads oscillations in this region, particularly apparent in pitching moment data. Surface streamline traces (oil flow) on the blades show the swept flow around the azimuth. Reversed flow is seen inboard on the retreating blade, otherwise there is no separation present.

Fuselage Effects

The overset methodology makes adding a fuselage a straightforward task. A low fidelity fuselage geometry (Figure 4) has been included in the coarse grid

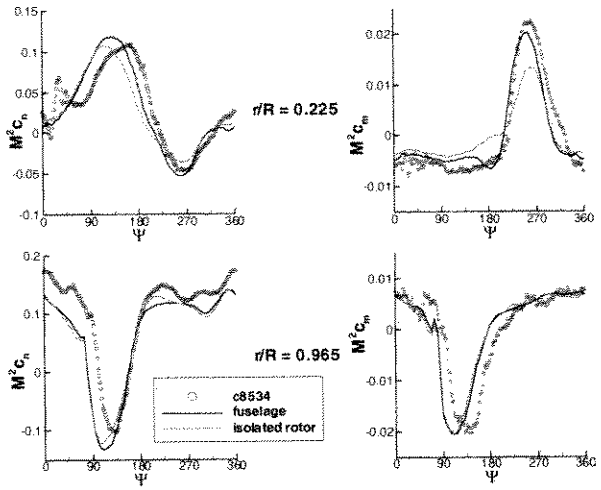

Figure 15. Fuselage effects, μ = 0.37

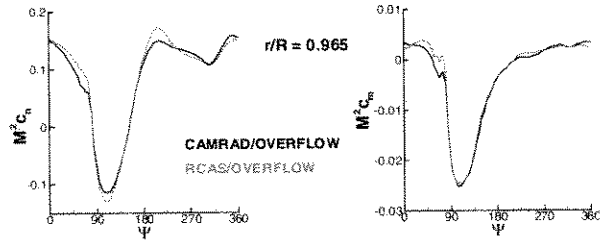

Figure 16. Comprehensive code comparison, μ = 0.37

calculation. Airloads with and without the fuselage are compared with the flight test data in Figure 15. It is seen that the primary effect is to induce an upwash on the inboard part of the rotor blade ($r/R < 0.40$) near 180 degrees azimuth, thereby increasing the normal force in this region. The change on this part of the rotor affects the overall trim equilibrium and results in a slight redistribution of forces everywhere on the rotor disk. Of note is the significant improvement in pitching moment comparison in the reversed flow region ($r/R = 0.225$, $\Psi \approx 270$ deg) due to the presence of the fuselage.

Comprehensive Code Coupling Modularity

To test the modularity of the coupling procedure, the Rotorcraft Comprehensive Analysis System (RCAS) [34] was substituted for CAMRAD II. RCAS is US Army developed software for predicting performance, stability and control, aeroelastic stability, loads and vibration, and aerodynamic characteristics of rotorcraft. A comparison of the coupled OVERFLOW/RCAS and OVERFLOW/ CAMRAD results are shown in Figure 16. The excellent agreement helps to validate the two structural models and implementation of the incremental coupling methodology.

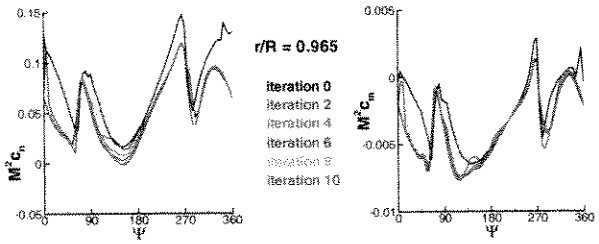

Figure 17. Airloads convergence, μ =0 .15

The differences are indicative of differing control system stiffnesses in the two structural models.

Low Speed

Flight counter c8513 is a low speed, $\mu = 0.15$, level flight data point. The freestream Mach number of this point is 0.096. At this condition there are significant blade-vortex interactions which dominate the airloads.

Coupling Convergence

Convergence of the coupling methodology occurs smoothly after 9 iterations on the baseline grid. Figure 17 shows that the last region to converge is the normal force on the outboard part of the blade around 180 degrees azimuth. The blade-vortex interactions actually converge quite quickly.

Data Comparison

Comparisons of the coupled OVERFLOW/ CAMRAD results with flight test data and CAMRAD II free wake analysis are shown in Figure 18 for representative span stations. Results are trimmed to measured thrust and shaft bending moment values. As with the high speed test point, the magnitudes of the normal force and pitching moment from the coupled solution are in excellent agreement with the flight test data, but in this case the phase agreement is also quite good. The magnitude and shape of the vibratory normal forces, 3/rev and higher, also show good agreement between the test data and analysis. Some of the details in the comparisons, such as minor oscillations and overshoots, are quite remarkable

The blade-vortex interaction normal force impulses at 90 and 270 degrees azimuth are captured accurately and sharply except for a slight phase shift. This is probably not the same phase shift mechanism as the high speed case. For the low speed case, the discrepancies could be caused by errors in wake location or excessive vortex dissipation. At $r/R = 0.675$, the blade-vortex interaction is underpredicted in the second quadrant.

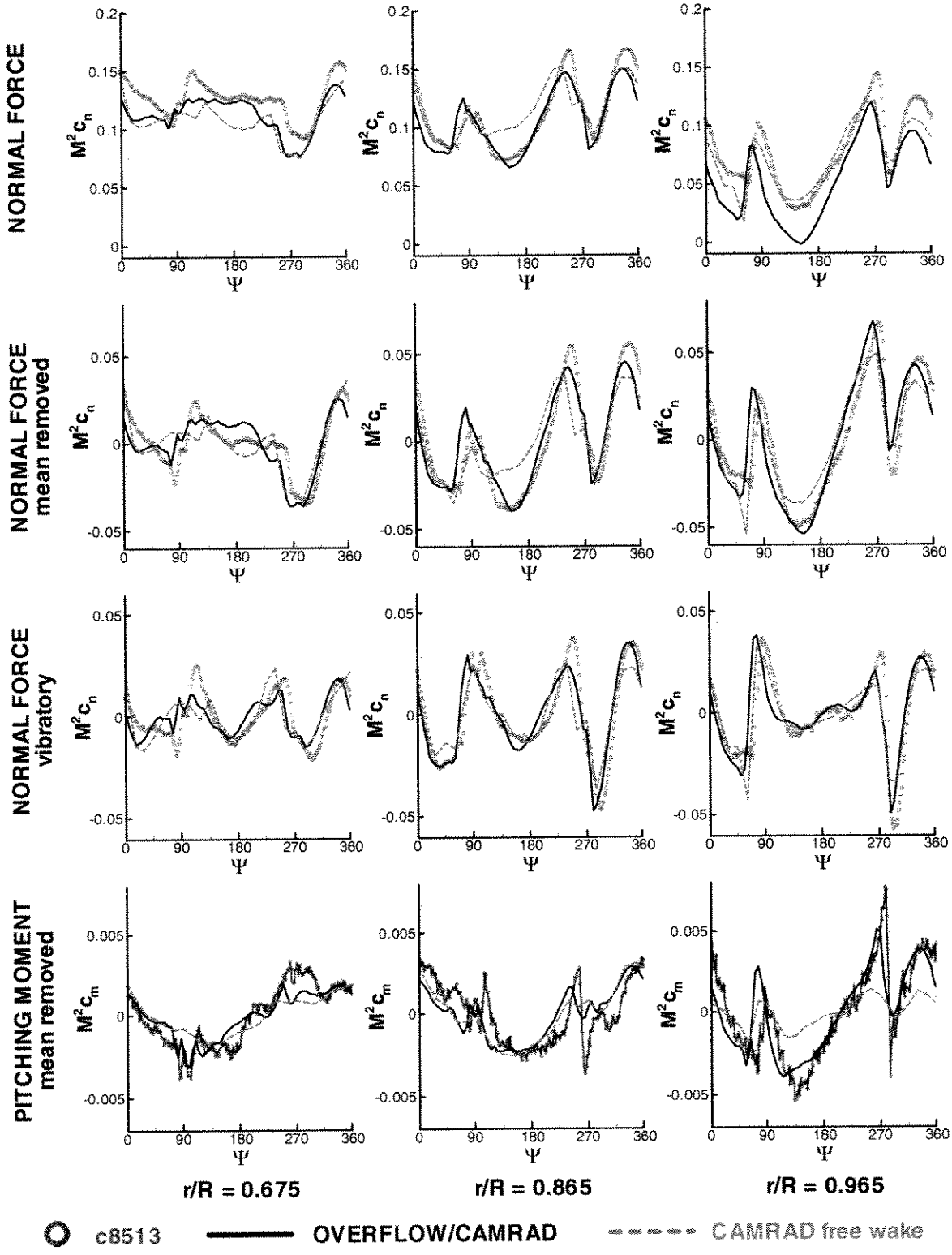

Figure 18. Airloads comparison, $\mu = 0.15$

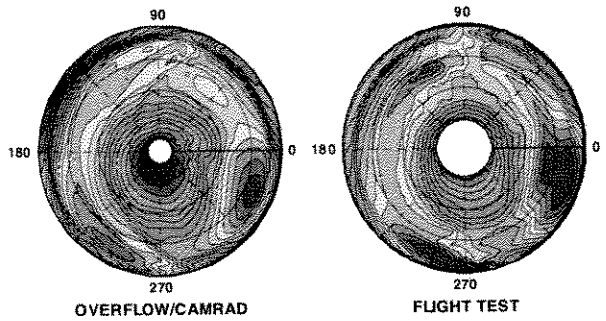

Figure 19. Rotor disk normal force comparison, $\mu = 0.15$

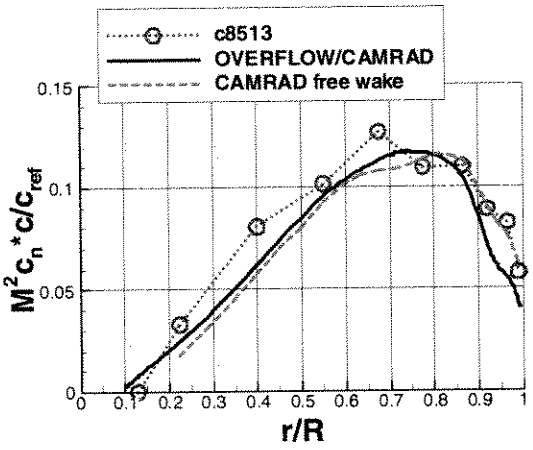

Figure 20. Mean normal force distribution, $\mu = 0.15$

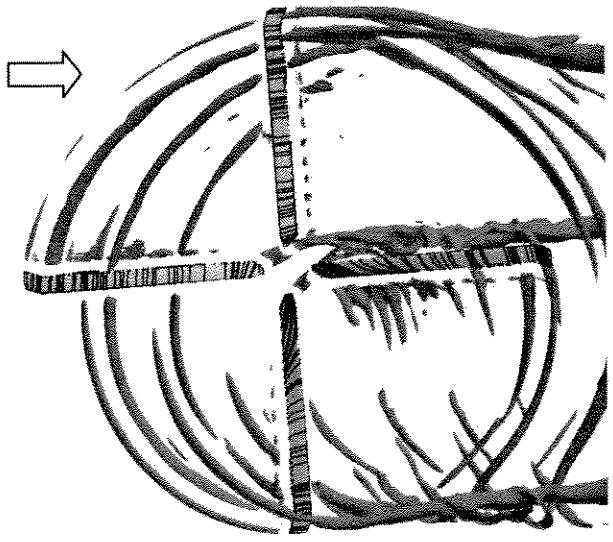

Figure 21. Wake visualization and surface streamlines, $\mu = 0.15$

Although the free wake analysis is acceptable for this flight condition, the coupled solution still shows an improvement in the shape of the curves, particularly in the second quadrant. The pitching moments are somewhat improved. Unlike the free wake analysis, the coupled analysis begins to capture the pitching moment impulse at r/R = 0.965 and Ψ = 270 degrees, but both are smeared out at r/R = 0.865.

Qualitative comparisons of normal force on the rotor disk are shown in Figure 19. The overall comparison is quite good, although the flight test data is at consistently higher levels. The most apparent difference is the high normal force region near r/R = 0.65 and Ψ = 120 degrees in the test data. In both plots the strong blade-vortex interaction impulses outboard on the advancing and retreating blades are well defined.

Comparisons of the coupled, free wake, and experimental mean normal force distributions are shown in Figure 20. Clearly, the coupled and free wake solutions trimmed to the measured thrust ($C_T/\sigma = 0.076$) are not generating the same thrust as the integrated airloads ($C_T/\sigma = 0.087$). The CAMRAD II free wake analysis matches the outboard, swept tip loading much better, but this implies even larger disagreement with the inboard test data. When this mean discrepancy is removed from the normal force comparisons, the agreement between test and coupled analysis is even more noteworthy (Figure 18).

Wake Visualization

Visualization of the wake in Figure 21 shows multiple blade-wake interactions. Wake structures in the second and third quadrants can be matched up with the normal force distributions in Figure 19. Inaccurate correlation with the blade-vortex interaction near r/R = 0.65 and Ψ = 120 degrees in the test data, however, indicates that some wake structures may not be correctly captured. Several tip vortices from the different blades are visible, but generally more than one revolution cannot be maintained in the off-body grids. For this low speed condition, the lag angle is reduced. The roll-up of the wake vortices into the super vortices are more evident than in the high speed calculation. As would be expected, no stall is present in the streamlines.

Grid Effects

Surprisingly, there are no airloads differences seen in the coarse grid results (not shown) other than a slight reduction in the peaks of the impulses from the blade-vortex interactions. It was unexpected that either grid, with wake grid spacings on the order of a physical tip vortex core, would have been able to accurately resolve the wake interactions with the blades. An even finer off-

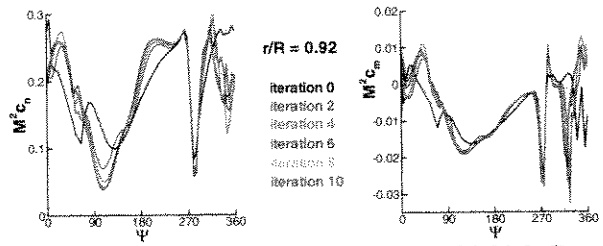

Figure 22. Airloads convergence, μ =0 .24, high C_T

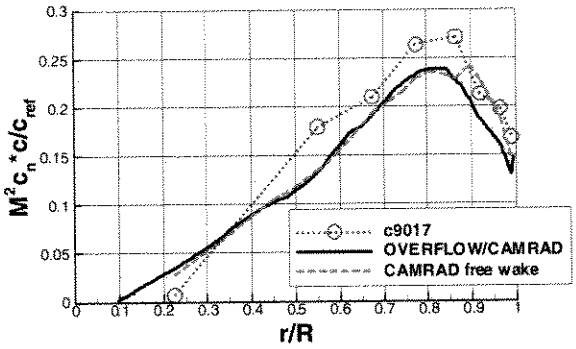

Figure 23. Mean normal force distribution, μ = 0.24, high C_T

body grid was generated with level-1 spacing of 0.05 chords, in conjunction with the baseline near-body grid system. Results from that calculation using the coupled, baseline grid motions still show no significant effects due to wake resolution. Although the comprehensive analysis results for the UH-60A low speed flight condition are highly dependent on the wake model and core size used [4], the CFD, on the other hand, seems insensitive to attempts to improve the solutions through reduced numerical viscosity or grid refinement. This is probably a result of the fact that the actual vortex cores are in no sense physically resolved.

High Thrust

Flight counter c9017 is an intermediate speed, $\mu = 0.24$, high thrust, level flight test point flown at 17,000 ft. The freestream Mach number is 0.157, and the hover tip Mach number has increased to 0.665. This is a challenging and quintessential rotorcraft test case due to the wide variation of unsteady flow conditions, ranging from transonic to stall, with noticeable wake interactions. The dynamic stall characteristics of this test point have previously been discussed in detail [35].

Coupling Convergence

Convergence of the coupling methodology occurs after 10 iterations on the baseline grid. One might suspect that if any conditions would have coupling convergence difficulties it would be a case with highly unsteady phenomena such as dynamic stall. The coupling convergence history in Figure 22, however, appears well behaved, and no changes in coupling strategy or frequency are required. The dynamic stall is repeatable at each quarter revolution and is not particularly sensitive to the trim iterations. A region of flow around 0 degrees azimuth continues to show small variations.

Data Comparison

Comparisons of the coupled, free wake, and experimental mean normal force distributions along the span are shown in Figure 23. Even worse than the previous two cases, the experimental mean normal force is systematically too high everywhere. The integrated thrust ($C_T/\sigma = 0.147$) is 13% higher than the measured thrust ($C_T/\sigma = 0.129$). The coupled and comprehensive free wake distributions are in reasonable agreement, although the comprehensive span loading is higher mid-span and at the tip due to lower levels of stall in these regions.

Comparisons of the coupled OVERFLOW/ CAMRAD results and CAMRAD II free wake analysis with flight test data are shown in Figure 24 for representative span stations. Overall, the agreement between flight test and coupled results is respectable, although not as good as the previous cases. Around the azimuth a constant 20 degree phase shift exists. The shape of the airloads, especially the pitching moments, are actually in very good agreement with the test data when the phase lag is ignored. On the advancing side the minimum peak loading phase lag discrepancy is of similar magnitude to the high speed test point lag. The dynamic stall encounters, evidenced by the large negative pitching moments, are also initiated too early. The global phase shift may be caused by incorrect prediction of the dynamic stall location. Changing the location of the initial stall event will effect the location of future stall events due to torsional overshoot. These changes on the retreating side retrim the rotor, affecting the advancing side airloads.

On the advancing side, the phase of the CAMRAD II multiple trailer wake with dynamic stall results are actually a small improvement over the coupled results. This may indicate that the phase lag mechanism seen in the high speed test case is not present. The CAMRAD II results show reasonable agreement with flight test data on the advancing side at $r/R = 0.675$ with worse magnitude agreement outboard. Stall regions are captured but with incorrect phase and magnitude. The results are a noticeable improvement over previous results using a rolled-up wake [2].

Other than the phase shift, the major discrepancies between flight test and the OVERFLOW/CAMRAD

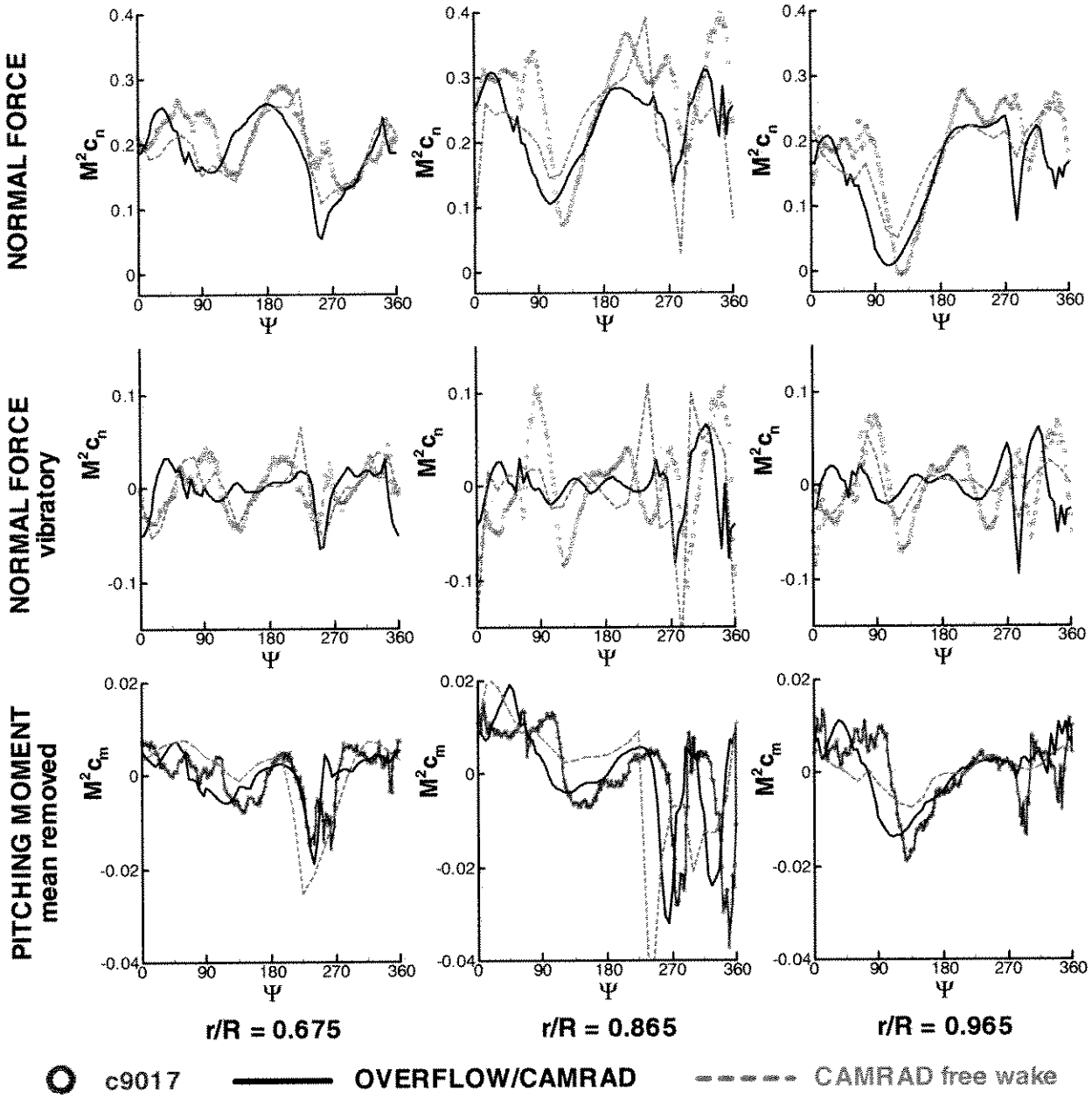

Figure 24. Airloads comparison, $\mu = 0.24$, high C_T

coupled solution are in normal force prediction on the outboard part of the blade. On the advancing side there is considerable disagreement in the steepness with which the minimum peak loading region is entered and departed. The normal force distributions also lack the higher level and overshoot oscillations in the third quadrant from 220 to 270 degrees azimuth. In comparison, the comprehensive free wake analysis somewhat captures the overshoot oscillations at the end of the third quadrant. Based on the wake visualization in Figure 25, this overshoot and oscillation could be a blade-vortex interaction that is poorly captured.

From the airloads plots, the extent of the calculated stall regions generally correspond to the flight test regions, with some underprediction of the spanwise extent at r/R = 0.775 (not shown) and 0.965. However, the flight test data shown are only the first revolution, and other revolutions indicate varying extent of the unsteady, non-

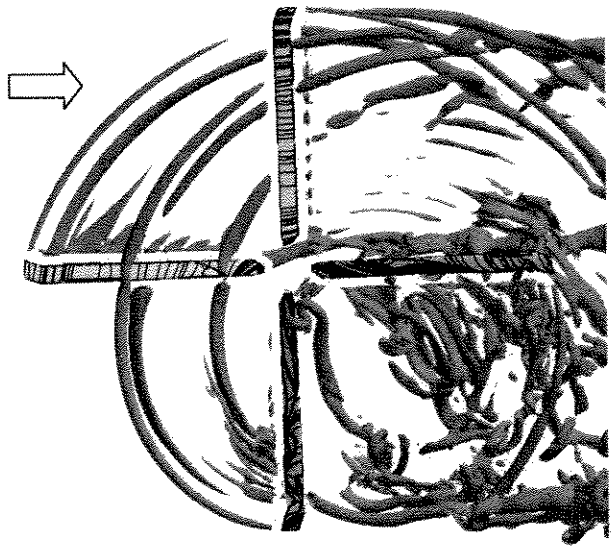

Figure 25. Wake visualization, surface streamlines, chordwise skin friction (— $c_f = 0$), $\mu = 0.24$, high C_T

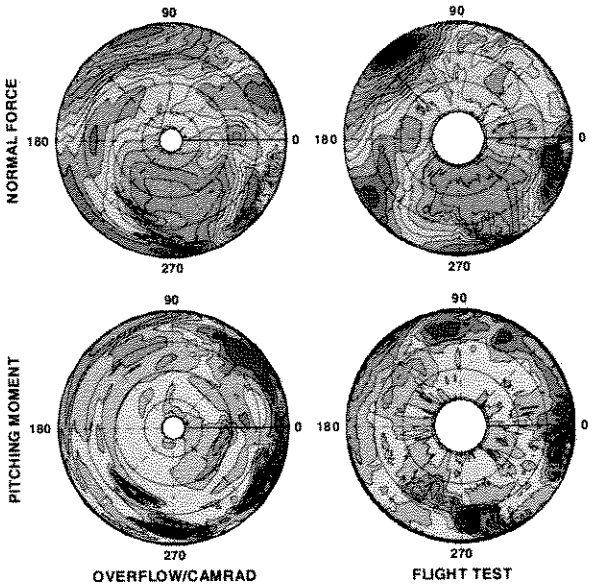

Figure 26. Rotor disk airloads comparison (mean removed), $\mu = 0.24$, high C_T

periodic, stall. The pitching moments in the stalled region show good oscillatory magnitude for prediction of pitch link loads at this level flight test point.

Qualitative comparisons of normal force and pitching moment on the rotor disk from the OVERFLOW/ CAMRAD coupled analysis and flight test are shown in Figure 26. Because of data offsets at some flight test stations for both normal force and pitching moment, the mean distribution has been removed. Except for the constant phase lag around the disk the comparison is, in general, quite good. As first indicated by the line plots, pitching moment is in especially good agreement, with all major features duplicated in the analysis. Normal force comparisons in the first quadrant are poor. The second quadrant indicates a computed minimum peak loading region that is larger in extent azimuthally but smaller radially.

Stall Regions

Several criteria can be used to detect separation or stall: section normal force break, section pitching moment break, trailing edge pressure divergence, surface streamlines, and chordwise skin friction.

In Figure 26 regions of stall on the rotor disk are apparent in the pitching moment and normal force as abrupt reductions in these quantities (blue). The progression is from mid-span to outboard for the first dynamic stall cycle. The second stall cycle is confined to the outboard section ($r/R > 0.75$). The normal force and pitching moment are consistent in their predictions, although the pitching moment seems especially sensitive and more useful for analysis.

Using the various stall detection criteria, a dynamic stall rotor map is created in Figure 27. All criteria are somewhat subjective. Stall initiation lines based on normal force and pitching moment gradients are indicated by green and blue, respectively. Regions of separation based on 96% chord upper surface pressure coefficient divergence of –0.06 from the mean are shaded. Zero chordwise skin friction at $x/c = 0.96$ is indicated in red. There is general agreement among all the stall/separation criteria. The skin friction criteria also identifies some of the reversed flow region.

The stall rotor map developed from the CFD solution is compared with that from flight test [35]. Taking into account a constant 20 degree phase shift of the entire solution, the dynamic stall regions are in remarkable agreement. The only discrepancy is the inboard extent of the second cycle and the disconnect between the two CFD regions there. It seems there is only mild stall inboard of $r/R = 0.75$, based on inconsistencies between the normal force, pitching moment, and pressure coefficient criteria in both analysis and flight test.

The wake visualization in Figure 25 shows considerable vortical flow in the 4th quadrant due to the stall structures. Surface streamlines (simulated oil flow) in this figure help to locate the separation regions around the disk. The zero contour of chordwise skin friction is shown in blue to highlight areas of reversed flow on the blade. At 270 degrees azimuth, in addition to the reversed flow region inboard, various separated regions extend from

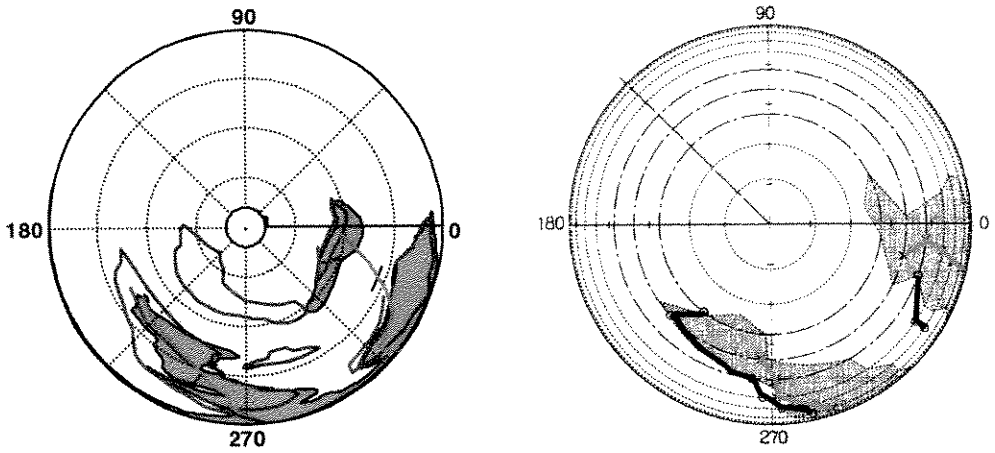

OVERFLOW/CAMRAD **FLIGHT TEST [35]**

Figure 27. Comparison of dynamic stall rotor maps, $\mu = 0.24$, high C_T
lift stall, moment stall, upper surface x/c = 0.96: pressure coefficient, skin friction

approximately r/R = 0.50 out to 0.90, although the flow is quite complicated. At 0 degrees azimuth separate mid-span and tip separation regions exist.

At 180 degrees azimuth two separation regions are identified by the streamlines and zero chordwise skin friction. The outboard area is determined to be a small leading edge separation bubble with reattachment immediately behind it, as indicated by some streamline traces which appear. There is also a small but well defined separation region inboard (0.26 < r/R < 0.33) at 180 degrees azimuth that extends to the trailing edge. Neither of these regions are indicated by the normal force, pitching moment, or surface pressure coefficient criteria on the stall rotor maps. It is interesting to note that the flight test stall rotor maps for high load factor maneuvers (pull-up or diving turn) [35] show that at increased load factors the dynamic stall next occurs between r/R = 0.25 and 0.40 at 180 degrees azimuth. Although this may be attributed to fuselage induced upflow, the CFD calculation already hints at a tendency for the flow to separate in this region.

Grid Effects

The high thrust, dynamic stall test point does show some sensitivity to grid density. This is not surprising as it is well known that CFD stall prediction can be highly grid dependent. Figure 28 shows grid density effects on the

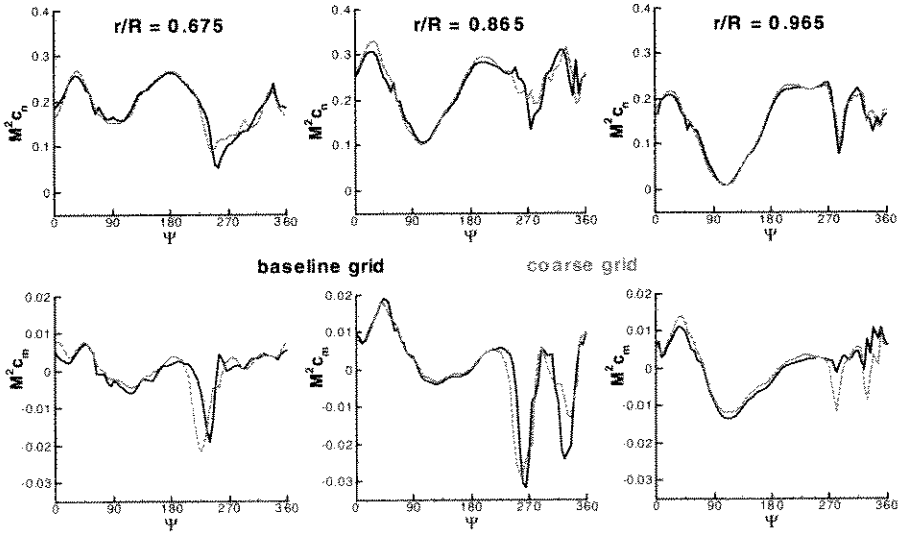

Figure 28. Grid convergence, $\mu = 0.24$, high C_T

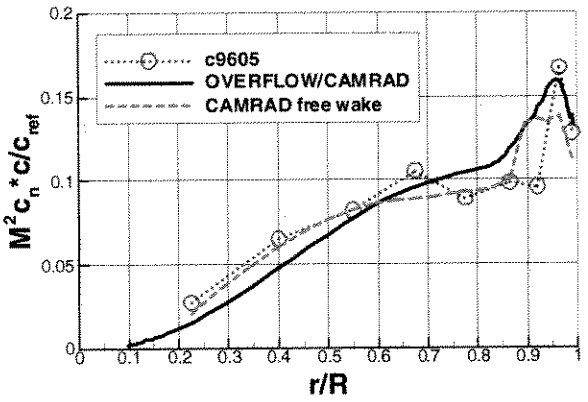

Figure 29. Mean normal force distribution, hover

airloads. At r/R = 0.675 and 0.865, the coarse grid shows earlier separation on the retreating blade than the baseline grid. Pitching moment magnitudes, i.e. separation severity and extent, are the same or reduced. At r/R = 0.965, the coarse grid moment stall is increased, fortuitously in better agreement with flight test, even though the lift stall remains the same. And yet, at other stations (not shown) there are no changes. This indicates that the phase shift, at least on the retreating side of the rotor, is sensitive to computational modeling details (turbulence model, grid density, numerical viscosity) causing premature stall. Recall that the high speed advancing side phase shift phenomenon does not seem dependent on these modeling parameters. Changes in the stall location on the retreating side and resulting retrim have not significantly affected the advancing side airloads.

It must be cautioned that further validation is required for this flight condition as CFD is notoriously fickle in predicting stall. Even though two-dimensional CFD has shown good correlation in predicting static stall for the UH-60 SC1095 airfoil [32], 2D and 3D dynamic stall predictions are an area of ongoing research for which CFD has not yet been validated. A more accurate and advanced turbulence model than Baldwin-Barth should be investigated. For overall stall prediction, however, the coupled, turbulent, Navier-Stokes results are an improvement over table look-up with dynamic stall modeling.

Hover

Flight counter c9605 is a hover point taken for ground acoustics measurements. The hover tip Mach number is 0.650. For this case, the integrated thrust level ($C_T/\sigma = 0.077$) is used as the trim target instead of the measured thrust ($C_T/\sigma = 0.069$), however, this value is certainly too high as it gives unreasonable estimates for airframe download. Non-zero hub moments are taken from flight test. The wind speed was less than 3 knots. The flight test data from this point have not received the thorough scrutiny given to the other test points used here. In general, inherent unsteadiness in the wake, wind, and tail rotor effects make reliable and repeatable hover data particularly challenging to obtain [29,36].

Although no-wind hover is most efficiently calculated using steady-state CFD methods, the coupling methodology is demonstrated here using the same unsteady, moving blade CFD formulation as for forward flight. In order to better capture the wake, the level-1off-body grid has been extended to -0.5R in z. A centerbody has been added to prevent flow recirculation at the blade roots. Results were obtained only on the coarse grid, so grid converged airloads prediction is not expected. Strawn [19] has shown that for a UH-60 model rotor in hover even wake spacings of 0.05 chords do not result in converged normal force distributions. This case is used mainly for demonstration purposes.

Coupling Convergence

Convergence of the CFD solution slows considerably for unsteady hover compared with forward flight. The wake is slow to develop and convect down, and wake details have a major effect on the blade airloads. Several rotor revolutions, at least 3, are required initially to set up the wake to an approximate degree. A more reasonable approach would be to use steady-state hover methods to initialize the solution, although that was not done here. Because of the increased influence of the wake, the coupling frequency was also changed from 90 degrees to a complete 360 degree revolution. Nonetheless, the coupling converges without difficulty after 10 iterations (rotor revolutions) for trim target, controls, and airloads.

Data Comparison

Comparisons of the coupled, free wake, and experimental mean normal force distributions along the span are shown in Figure 29. The CAMRAD II free wake analysis shows good agreement with the flight test data, with an underprediction of the maximum outboard peak loading. The agreement between the flight test data and the coupled solution is not particularly good, with redistribution of loading from inboard to outboard. Neither analysis captures the peakedness of the outboard loading, which is due to the first blade vortex passage. The coupled calculation is in better agreement with computations and model test data from Strawn [19]. Finer wake spacings would tend to narrow the outboard peak and increase the maximum peak loading in the CFD calculation.

Computational Cost

All solutions were run on an IBM pSeries 690 parallel supercomputer with 1.4 GHz Power4 processors. The baseline grid was run on 80 processors and required 4.7 hours per coupling iteration (90 degrees of revolution). The coarse grid, however, requires only 16 processors and 2.0 hours per coupling iteration in forward flight. Therefore, a converged, coupled, coarse grid solution for airloads prediction can be obtained from scratch in approximately 20-28 wallclock hours, or 12-20 hours if flow solver restart capability is used at the start of the coupling. While still too expensive for design work, coupled CFD and comprehensive analysis of forward flight rotor configurations is quickly approaching the point where a reasonable matrix of test points could be run on desktop processors.

CONCLUSIONS

A Navier-Stokes CFD code OVERFLOW-D has been loosely coupled on a per revolution, periodic basis with a rotorcraft comprehensive code CAMRAD II. The CFD models the complete helicopter configuration using turbulent, viscous flow and a first principles-based wake. CFD aerodynamics (normal force, pitching moment, and chord force) are applied in the comprehensive code using an incremental, iterative methodology for trim and aeroelastics. A complete range of level flight conditions, high speed with advancing blade negative lift, low speed with blade-vortex interactions, high thrust with dynamic stall, and hover, has been demonstrated. Airloads have been compared with data from the UH-60A Airloads Program and state-of-the-art comprehensive free wake analysis. Wake visualizations and rotor stall maps were extracted from the CFD solutions to show flowfield details. The following conclusions are made from the results presented:

1) Loose coupling is efficient and robust for a wide range of helicopter flight conditions. All the force and moment components (normal force, pitching moment, and chord force) can be coupled without convergence problems.
2) CFD/comprehensive coupled analysis can be a significant improvement over comprehensive lifting line aerodynamics with free wake and dynamic stall models. Normal force and pitching moment magnitudes are accurately captured in the coupled solutions.
3) Although generally improved over comprehensive analysis, phase lag of the airloads in coupled solutions when compared with test data remains a significant problem at some flight conditions. Ignoring the phase lag, the shape of the airloads curves is usually quite accurate.
4) The phase lag is predominantly caused by unknown mechanisms associated with high speed, negative lift on the advancing blade. Premature stall on the retreating blade, if present, and resulting retrim is also a factor. Unlike premature stall, the high speed phase lag is not associated with known CFD numerical issues such as grid density, turbulence modeling, or dissipation.
5) Comparison of results using two comprehensive and two CFD codes gives confidence in implementation of the aeroelastic and coupling methodologies.
6) Unknown, systematic differences between measured and integrated thrust and hub moments in the UH-60A airloads measurements make comparison of mean values and trim conditions problematic, although this is no different than many other experimental databases.

FUTURE WORK

Overall, these results show that CFD/comprehensive code coupling is fast becoming an attainable and accurate tool for the rotorcraft analyst, although considerable work remains. The CFD solutions provide a wealth of aerodynamic information that can be investigated for detailed flow phenomenon. Further calculations and detailed comparison of the CFD and comprehensive free wake results for the high speed test case should help resolve the problem of the phase lag discrepancy in high speed flight. Some rotors do not show the phase lag in comprehensive analysis [4], and it would be highly instructive to investigate these other datasets. Structural loads and blade motions from the comprehensive code using the CFD aerodynamics need to be compared with flight test data. For structural loads as well as performance prediction, the viscous component of the CFD airloads should be included. In spite of the success of the loose coupling, tight coupling should not be neglected.

ACKNOWLEDGEMENTS

This work would not have been possible without the computer resources of the Department of Defense Major Shared Resource Centers (MSRC) which are gratefully acknowledged. The authors also thank researchers at the University of Maryland for numerous useful discussions and opportunities for collaboration and comparison. In particular, Dr. Jayanarayanan Sitaraman provided the TURNS solution. Dr. Robert Ormiston helped with the RCAS coupling demonstration.

REFERENCES

1. Bousman, W. G., "Putting the Aero Back into Aeroelasticity," 8th ARO Workshop on Aeroelasticity of Rotorcraft Systems, University Park, PA, October 1999.

2. Nguyen, K. and Johnson, W., "Evaluation of Dynamic Stall Models with Flight Test Data," American Helicopter Society 54th Annual Forum, Washington, D.C., May 1998.

3. Lim, J. W., and Anastassiades, T., "Correlation of 2GCHAS Analysis with Experimental Data," *Journal of the American Helicopter Society*, Vol. 40, (4), October 1995, pp. 18-33.

4. Yeo, H. and Johnson, W., "Assessment of Comprehensive Analysis Calculation on Helicopter Rotors," American Helicopter Society 4th Decennial Specialists' Conference on Aeromechanics, San Francisco, CA, January 2004.

5. Altmikus, A. R. M., Wagner, S., Beaumier, P., and Servera, G., "A Comparison: Weak versus Strong Modular Coupling for Trimmed Aeroelastic Rotor Simulations," American Helicopter Society 58th Annual Forum, Montreal, Quebec, June 2002.

6. Pomin, H. and Wagner, S., "Aeroelastic Analysis of Helicopter Blades on Deformable Chimera Grids," AIAA Paper 2002-0951, AIAA 40th Aerospace Sciences Meeting and Exhibit, Reno, NV, January 2001.

7. Tung, C., Caradonna, F. X., and Johnson, W. R., "The Prediction of Transonic Flows on an Advancing Rotor," American Helicopter Society 40th Annual Forum, Arlington, VA, May 1984.

8. Kim, K-C., Desopper, A., and Chopra, I., "Blade Response Calculations Using Three-Dimensional Aerodynamic Modeling," *Journal of the American Helicopter Society*, Vol. 36, No. 1, pp. 68-77, January 1991.

9. Strawn, R. C., Desopper, A., Miller, M., and Jones, A., "Correlation of PUMA Airloads – Evaluation of CFD Prediction Methods," Paper No. 14, 15th European Rotorcraft Forum, Amsterdam, Netherlands, September 1989.

10. Strawn, R. C. and Bridgeman, J. O., "An Improved Three-Dimensional Aerodynamics Model for Helicopter Airloads Prediction," AIAA Paper 91-0767, AIAA 29th Aerospace Sciences Meeting and Exhibit, Reno, NV, January 1991.

11. Beaumier, P., "A Coupling Procedure Between a Rotor Dynamics Code and a 3D Unsteady Full Potential Code," American Helicopter Society 3rd Decennial Specialists' Conference on Aeromechanics, San Francisco, CA, January 1994.

12. Servera, G., Beaumier, P., and Costes, M., "A Weak Coupling Method Between the Dynamics Code HOST and the 3D Unsteady Euler Code WAVES," 26th European Rotorcraft Forum, The Hague, Netherlands, September 2000.

13. Sitaraman, J., Baeder, J., and Chopra, I., "Validation of UH-60A Rotor Blade Aerodynamic Characteristics Using CFD," American Helicopter Society 59th Annual Forum, Phoenix, AZ, May 2003.

14. Sitaraman, J., Datta, A., Baeder, J. D., and Chopra, I., "Fundamental Understanding and Prediction of Rotor Vibratory Loads in High-Speed Forward Flight," 29th European Rotorcraft Forum, Friedrichshafen, Germany, September 2003.

15. Pahlke, K. and van der Wall, B., "Calculation of Multibladed Rotors in High-Speed Forward Flight with Weak Fluid-Structure-Coupling," 27th European Rotorcraft Forum, Moscow, Russia, September 2001.

16. Datta, A., Sitaraman, J., Chopra, I., and Baeder J., "Improved Comprehensive Analysis for Prediction of Rotor Vibratory Loads in High-Speed Forward Flight," American Helicopter Society 60th Annual Forum, Baltimore, MD, June 2004.

17. Johnson, W., "Rotorcraft Aerodynamic Models for a Comprehensive Analysis," American Helicopter Society 54th Annual Forum, Washington, D. C., May 1998.

18. Chan, W. M., Meakin, R. L., and Potsdam, M. A., "CHSSI Software for Geometrically Complex Unsteady Aerodynamic Applications," AIAA Paper 2001-0593, AIAA 39th Aerospace Sciences Meeting and Exhibit, Reno, NV, January 2001.

19. Strawn, R. C. and Djomehri, M. J., "Computational Modeling of Hovering Rotor and Wake Aerodynamics," American Helicopter Society 57th Annual Forum, Washington, DC, May 2001.

20. Potsdam, M. A. and Strawn, R. C., "CFD Simulations of Tiltrotor Configurations in Hover," American Helicopter Society 58th Annual Forum, Montreal, Quebec, June 2002.

21. Meakin, R. L., "Automatic Off-Body Grid Generation for Domains of Arbitrary Size," AIAA Paper 2001-2536, 15th AIAA Computational Fluid Dynamics Conference, Anaheim, CA, June 2001.

22. Meakin, R. L., "Object X-Rays for Cutting Holes in Composite Overset Structured Grids," AIAA Paper 2001-2537, 15th AIAA Computational Fluid Dynamics Conference, Anaheim, CA, June 2001.

23. Thomas, P. D. and Lombard, C. K., "Geometric Conservation Law and Its Application to Flow Computations on Moving Grids," *AIAA Journal*, Vol. 17, No. 10, 1979, pp. 1030-1037.

24. Farhat, C., Geuzine, P., and Grandmont, C., "The Discrete Geometric Conservation Law and its Effect on Nonlinear Stability and Accuracy," AIAA Paper 2001-2607, 15th AIAA Computational Fluid Dynamics Conference, Anaheim, CA, June 2001.

25. Obayashi, S., "Freestream Capturing for Moving Coordinates in Three Dimensions," *AIAA Journal*, Vol. 30, No. 4, 1992, pp. 1125-1128

26. Morton, S. A., Melville, R. B., and Visbal, M. R., "Accuracy and Coupling Issues of Aeroelastic Navier-Stokes Solutions on Deforming Meshes," *Journal of Aircraft*, Vol. 35, No. 5, 1998, pp. 798-805.

27. Bauchau, O. A. and Ahmad, J. U., "Advanced CFD and CSD methods for Multidisciplinary Applications in Rotorcraft Problems," AIAA/NASA/ISSMO Symposium on Multidisciplinary Analysis and Optimization, Bellevue, WA, September 1996.

28. Kufeld, R. M., Balough, D. L., Cross, J. L., Studebaker, K. F., Jennison, C. D., and Bousman, W. G., "Flight Testing of the UH-60A Airloads Aircraft," American Helicopter Society 50th Annual Forum, Washington, D.C., May 1994.

29. Bousman, W. G. and Kufeld, R. M., "UH-60A Airloads Catalog", NASA TM, to be published, 2004.

30. Ormiston, R. A., "An Investigation of the Mechanical Airloads Problem for Evaluating Rotor Blade Structural Dynamics Analysis," American Helicopter Society 4th Decennial Specialists' Conference on Aeromechanics, San Francisco, CA, January 2004.

31. Lorber, P. F., "Aerodynamic Results of Pressure-Instrumented Model Rotor Test at the DNW," *Journal of the American Helicopter Society*, Vol. 36, No. 4, October 1991, pp. 66-76.

32. Smith, M. J., Wong, T.C., Potsdam, M. A., Baeder, J., and Phanse, S., "Evaluation of CFD to Determine Two-Dimensional Airfoil Characteristics for Rotorcraft Applications," American Helicopter Society 60th Annual Forum, Baltimore, MD, June 2004.

33. Jeong, J. and Hussain, F., "On the Identification of a Vortex," *Journal of Fluid Mechanics*, Vol. 285, 1985, pp. 69-94.

34. Saberi, H., Khoshlahjeh, M., Ormiston, R. A., and Rutkowski, M. J., "Overview of RCAS and Application to Advanced Rotorcraft Problems," American Helicopter Society 4th Decennial Specialists' Conference on Aeromechanics, San Francisco, CA, January 2004.

35. Bousman, W. G., "A Qualitative Examination of Dynamic Stall from Flight Test Data," American Helicopter Society 53rd Annual Forum, Virginia Beach, VA, April 1997.

36. Shinoda, P., Yeo, H., and Norman, T., "Rotor Performance of a UH-60 Rotor System in the NASA Ames 80- by 120-Foot Wind Tunnel," American Helicopter Society 58th Annual Forum, Montreal, Canada, June 2002.